Quantum dots in microcavities: from single spins to engineered states of light
Steindl, P.

2 Cavity-QD device with an electron blocking layer

For the research in this thesis, we use self-assembled quantum dots embedded in optical microcavities with a cavity design originally developed for semiconductor lasers [56–58] (and Ph.D. theses [59–61]). The cavity is formed by two distributed Bragg reflectors (DBR) around a λ-thick active region of a *p-i-n* junction containing semiconductor quantum dots (QDs) and a $3/4\lambda$-thick oxide aperture. For this research, the design was adopted with a small change in the diode active region, allowing deterministic QD spin loading due to an added electron-blocking layer. In this chapter, we discuss the optical properties of devices with this blocking layer and discuss experimental techniques we use to determine the spin state and certify the single-photon emission of our QDs.
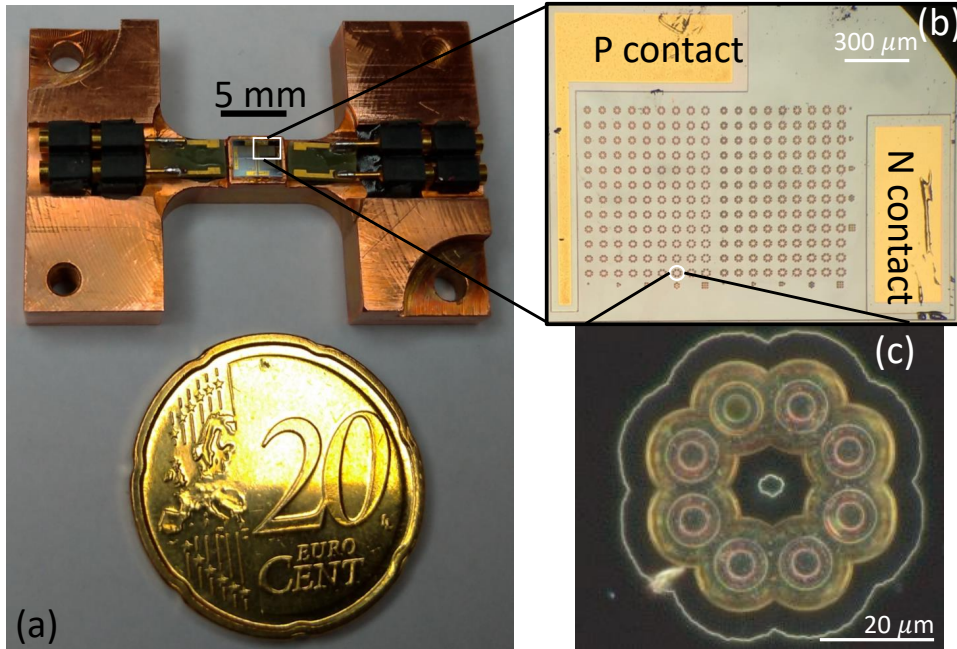
2.1 Cavity design

Figure 2.1: Optical images of the sample. (a) A photograph of the sample glued on the sample holder. (b) An optical microscope image of one-quarter of the semiconductor chip containing over 200 micropillar cavities. (c) Top view dark optical image of a cavity device after etching away the top DBR with eight etched trenches forming an octagon shape oxide aperture.

Images of the sample used in this thesis are shown in Fig. 2.1. Figure 2.1(a) is an optical image of the sample holder with the semiconductor chip glued on top and electrically connected through gold wire bonds to electric contacts. Figure 2.1(b) shows an optical-microscope image of one-quarter of the chip with over 200 micropillar cavities with common electrical contacts. Panel (c) shows the top view on a cavity device with eight holes etched in an octagon shape into the top cavity mirror. Due to refractive index contrast, we easily distinguish the oxide aperture from the cavity center.

Figure 2.2(a) shows the cross-sectional plot of the micropillar design. The top DBR mirror is composed of 26 pairs of $\lambda/4$-thick layers of GaAs and $Al_{0.9}Ga_{0.1}As$, while the bottom mirror consists of 13 pairs of layers of GaAs and AlAs and 16 pairs of GaAs and $Al_{0.9}Ga_{0.1}As$ layers. The oxide aperture used to increase in-plane light confinement (due to the reduction of refractive index from $n \approx 3$ to $n \approx 1.5$) to the center of the cavity is prepared by wet oxidation of a 10-nm AlAs layer embedded in the p-rich layer [63, 64]. We use an octagon-shaped oxide aperture with eight holes which we also call trenches. On the chip, the distance between the trenches varies cavity-to-cavity by design, allowing the manufacture of oxide apertures of different diameters and ellipticities. Reduction of the aperture diameter yields smaller cavity mode volumes due to stronger transverse light confinement while varying ellipticity allows controlling the fundamental cavity mode splitting [64]. The QD layer is grown in an intra-cavity electric-field anti-node in the intrinsic region of the p-i-n junction at a position determined by transmission matrix method (TMM) calculations.

In Fig. 2.2(b), we show a polarization-resolved spectrum of cavity modes recorded
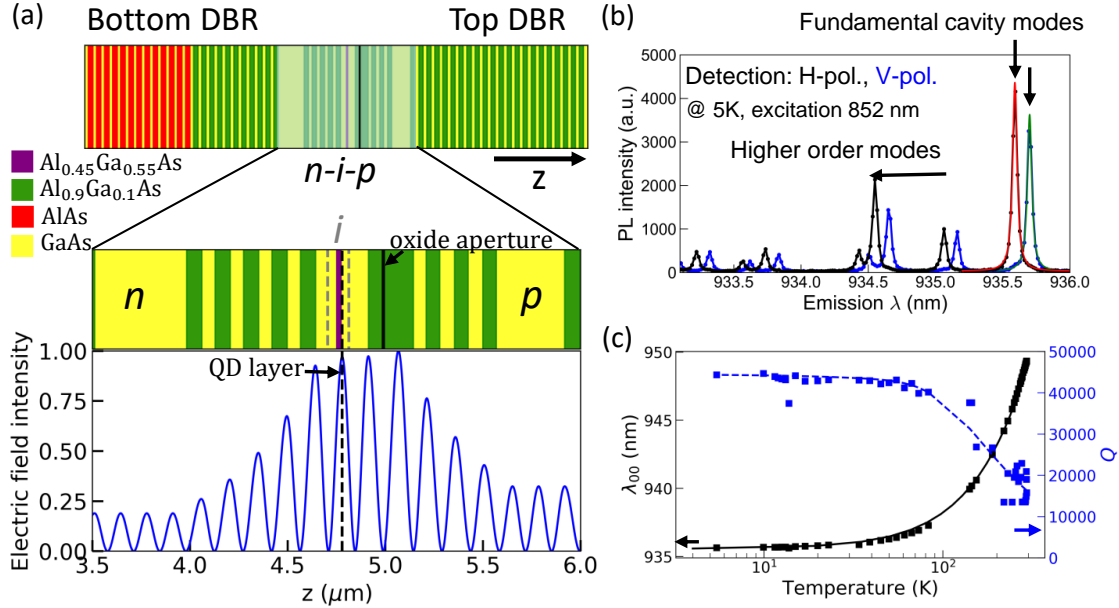
Figure 2.2: Micropillar cavity design and optical characterization. (a) TMM (transmission matrix method) cavity design with the calculated intra-cavity electric field. The gray dashed area shows the intrinsic part of the *p-i-n* junction, including the QD layer (dashed black line). (b) The spectrum of cavity modes was measured in two orthogonal linear polarizations. (c) The temperature-mediated shift of resonant wavelength λ_{00} (black) and Q factor (blue) of the fundamental cavity mode. Symbols: experiment, solid line: TMM calculation, dashed line: Q factor calculated assuming phonon broadening of the cavity resonance [62].

with a spectrometer [65]. We intentionally did not optimize the spatial coupling of the excitation laser to the micropillar cavity to also observe higher-order cavity modes. The fundamental cavity mode presented in Fig. 2.2(b) is split by shape- and strain-induced birefringence by $\sim 0.1\,\mathrm{nm}$ into two orthogonal linearly polarized modes (H and V). The cavity splitting was determined by a Lorentzian curve fit. Neglecting the mode-splitting, the measured resonant wavelength of about $935.5\,\mathrm{nm}$ agrees well with simple TMM calculation.

In Fig. 2.2(c), we confirm the device design by monitoring the fundamental mode wavelength λ_{00} and quality factor Q as a function of sample temperature. The wavelength λ_{00} shifts towards higher wavelengths due to material expansion at elevated temperatures and band-gap changes influencing the refractive index. We reproduce this shift with a simple temperature-dependent TMM simulation where the real part of the refractive index is temperature dependent because of shifts of the band gaps [66] and cavity expansion by lattice parameters [67]. We correct the modeled temperature dependence of λ_{00} in Fig. 2.2(c) by subtraction of $1.07\,\mathrm{nm}$. This correction is needed to account for other effects, such as band-gap changes induced by mechanical stress [68] created by multi-layer stacking or for a complex spatial profile of oxidation aperture. At $5\,\mathrm{K}$, we measure a Q factor of around $43\,000$, in good agreement with the simulations.

2.2 A QD in a micropillar cavity

2.2.1 Growth

We use self-assembled semiconductor QDs grown in Stranski-Krastanov growth mode with molecular-beam epitaxy [69, 70]. After the deposition of 1.5 monolayers of indium arsenide (InAs) on gallium arsenide (GaAs) buffer (at $500\,°$) [71], it becomes energetically favorable to form small nanometer-scale islands and thus partially release accumulated strain energy induced by material lattice mismatch. This self-organization simultaneously occurs at random positions on the wafer and leads to the assembly of few-nanometers high pyramid-shaped islands with high crystalline quality [72], the InGaAs quantum dots.

The GaAs matrix with a higher semiconductor band gap than InGaAs QDs serves as a three-dimensional potential barrier for charge carriers in the InGaAs, leading to the carrier localization within the In-rich region. The strong confinement of the carriers in the QD results in electron and hole state energy quantization responsible for sharp optical transitions between these discrete levels observed at cryogenic temperatures, similar to atoms [73].

Unlike in atoms, electronic states and optical properties of QDs can be tailored by the size, shape, and composition of the QDs and the surrounding material. We use this tunability during the final phase of the QD growth. First, the GaAs capping layer is deposited, limiting indium atom diffusion and ensuring both electron- and hole-carrier localization in the QD [74, 75]. Then, the composition and emission energy of QDs are adjusted by In-Ga atom intermixing driven by thermal annealing at $600\,°$ [76].

2.2.2 Electrical tuning of QD state

We embed a single layer of QDs in the active region of a *p-i-n* junction. Figure 2.3(a) shows a sketch of the *p-i-n* junction band scheme, where the red dashed line indicates the Fermi level. We can use the Fermi level adjustment by applying lateral bias voltage V_{G} to fine-tune the QD transition energy via the quantum-confined Stark effect. This effect was identified by Miller et al. [77], and it became a popular tool in the quantum dot community [78–82] to engineer the QD emission energy. The emission energy can be described by $E(F) = E_0 - pF - \beta F^2$, where p is the permanent electric dipole, β the polarizability of a QD with zero bias energy E_0 [80, 83]. Our *p-i-n* diode has a build-in voltage $V_{\mathrm{bi}} \approx 0.95\,\mathrm{V}$, resulting in an electric field $F = (V_{\mathrm{G}} - V_{\mathrm{bi}})/d$ in the intrinsic region of thickness $d \approx 142\,\mathrm{nm}$ [84]. Due to the build-in voltage, the flat-band condition ($F = 0\,\mathrm{kVcm^{-1}}$) is reached at $V_{\mathrm{G}} = V_{\mathrm{bi}}$. Figure 2.3(b) presents the Stark-shift of a single dot with $p = 7 \pm 1\,\mu\mathrm{eV}\,\mathrm{kV^{-1}cm}$, $\beta = 0.16 \pm 0.02\,\mu\mathrm{eV}\,\mathrm{kV^{-2}cm^2}$, $E_0 = 1318.0 \pm 0.1\,\mathrm{meV}$ - values typical for InGaAs QDs [84]. This control of the electronic energy levels is essential in cavity quantum electrodynamics for tuning the QD transition into resonance with the optical cavity [18, 85] or for control of photon indistinguishability from remote quantum emitters [26, 86, 87].

Depending on the total spin number of the QD ground state, QDs host a variety of excitonic states [88, 89]. Excitonic states of the main interest in this thesis are neutral excitons X^0 formed by a single excitation of initially empty QD and singly-charged excitons X^-, where the QD confines an extra electron before the excitation. Due to different spin configurations, these excitonic complexes also have distinct optical selection rules assisting the optical transitions: emission of a linearly polarized photon from X^0 and a photon of circular polarization from X^-. We show sketches of the optical selection rules
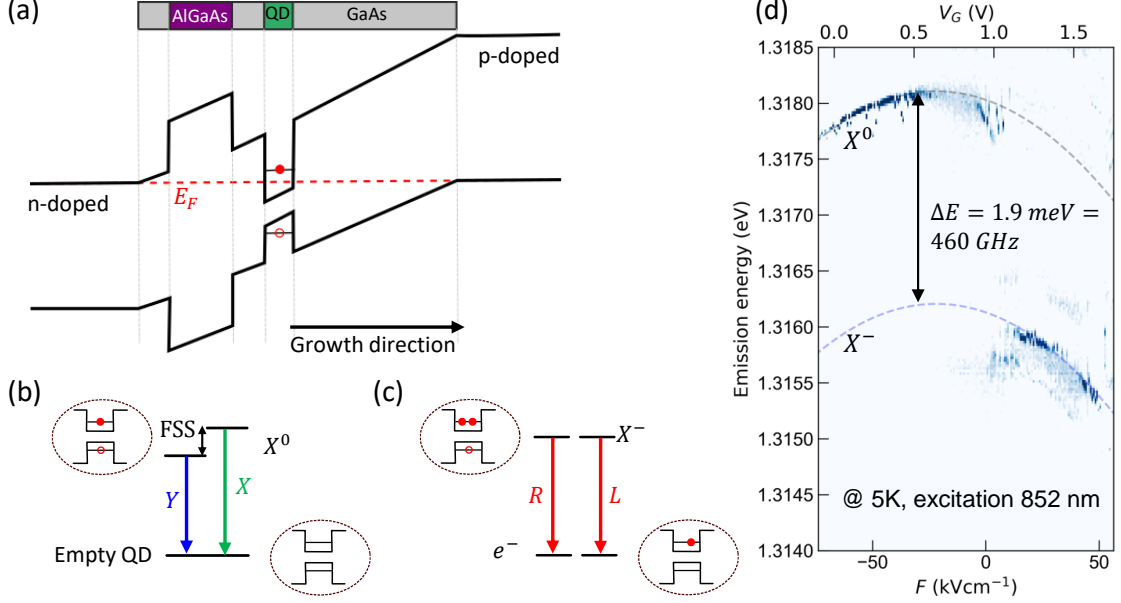
Figure 2.3: Electric field tuning of a QD transition: (a) Sketch of the band alignment in the *p-i-n* region of the micropillar cavity. Applying a bias voltage shifts the QD levels and allows for fine band-gap tuning. (b,c) Sketches of energy levels with optical selection rules of the neutral X^0 and negatively charged exciton X^-. Excess electrons (full circles) in the conduction band and holes (empty red circles) in the valence band are represented. (d) Voltage-induced tuning of the photon energy of a single QD resolved using off-resonant (excitation $\lambda = 852\,\mathrm{nm}$, $55\,\mu\mathrm{W}$) photoluminescence spectroscopy. Around $V_{\mathrm{G}} = 1\,\mathrm{V}$, we observe single-electron charging of the QD.

in Fig. 2.3(b,c). In fact, due to QD geometry, there are two orthogonally polarized neutral excitons (denoted as X, Y) separated by the fine structure splitting (FSS) energy. Previous studies of our QDs showed FSS energy between $2\,\mathrm{GHz}$ and $4\,\mathrm{GHz}$ [18, 90].

During sample growth, we included a $21.8\,\mathrm{nm}$ thick $\mathrm{Al}_{0.45}\mathrm{Ga}_{0.55}\mathrm{As}$ layer $5\,\mathrm{nm}$ below the QD layer [91, 92]. The combination of the bias control and the extra blocking layer allows for the deterministic trapping of an excess electron (a carrier in general) in the QD and the formation of the negatively charged exciton X^-. If the excess electron is trapped, the QD excitonic complex changes, resulting in a sudden step in the emission energy of the QD [93], while p and β defined dominantly by QD geometry are unchanged [94, 95]. Figure 2.3(d) shows a typical bias-resolved photoluminescence with parabolic dependence given by p and β, and an energy step of $\Delta E = 1.9\,\mathrm{meV}(= 460\,\mathrm{GHz})$ above $V_{\mathrm{G}} = 1\,\mathrm{V}$. This energy step is a signature of single-electron charging of a neutral exciton ($V_{\mathrm{G}} < 1\,V$) and formation of a negative trion ($V_{\mathrm{G}} > 1\,V$). The binding energy ΔE is in good agreement with trion binding energies reported in literature [88, 93, 96], supporting the identification of trion formation. Above $V_{\mathrm{G}} = 1\,\mathrm{V}$ (and below threshold voltage $V_{\mathrm{G}} = 1.52\,\mathrm{V}$ of GaAs at cryogenic temperature), the device works in the Coulomb blockade regime and provides extra spin to access single-spin physics and to implement a spin quantum memory [43].

2.3 Trion identification of QD spin-state configuration in the presence of an optical cavity

Typically, the distinct optical selection rules allow mapping of the polarization of an emitted photon to the QD spin-state configuration. Probably the simplest experiment to learn about polarization is to perform polarized photoluminescence spectroscopy of the QD. Here, the QD is excited non-resonantly with a laser, and the emission is analyzed as a function of linear polarization with a spectrometer with high spectral resolution [44, 97]. Unfortunately, being limited by the resolution of our spectrometer of around 6 GHz, this simple technique is challenging for direct discrimination between a single emission line of a trion and that of an exciton doublet with FSS, which is approximately two times smaller than the resolution. Instead, we use resonant excitation spectroscopy, where the spectral resolution is given by the continuous-wave narrow-linewidth laser, scanning across the cavity fundamental modes. Combining this technique with the control of additional parameters, we can identify the spin state and obtain other information about our system. We discuss several examples below.

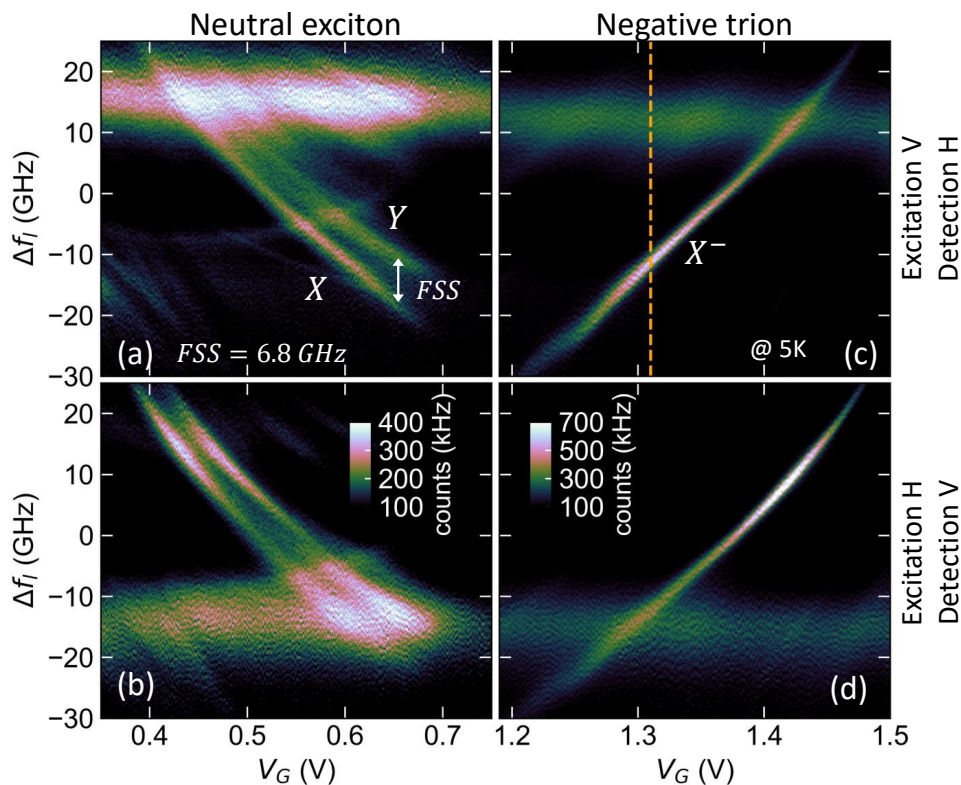### 2.3.1 Resonant Stark spectroscopy under cross-polarization

Figure 2.4: QD spin state identification using the Stark spectroscopy with cross-polarization technique. We show voltage scans of the neutral exciton (a,b) and negatively charged trion (c,d) measured in cross-polarization with excitation polarization aligned to V- (top panels) or H- (bottom) polarization of the fundamental cavity mode. The vertical line in (c) shows the bias voltage chosen later in the photon-correlation measurement, Fig. 2.7.

The birefringent cavities that we use have their fundamental resonant mode split by several GHz into two orthogonal linearly polarized modes. We typically associate the used polarization frame with these cavity modes and label them as H- and V-polarized cavity modes. Now, we focus on configurations where the excitation laser has polarization identical to one of the cavity modes. Then, the reflected laser light can almost perfectly be filtered out from the QD emission by cross-polarization filtering with detection polarization orthogonal to excitation. This technique requires fine-tuning of the excitation and detection polarizations which is discussed in detail in the next chapter. In this chapter, we focus only on state identification using this technique. In Fig. 2.4, we compare resonant Stark spectroscopy of neutral and charged excitons, presented in the left and right columns, respectively.

First, we comment on the neutral exciton transition shown in panels (a,b). We typically observe the neutral exciton transition at bias voltages $V_G < 1\,\mathrm{V}$, in agreement with the photoluminescence spectroscopy presented above. As expected for X^0, the resonant fluorescence reveals two emission lines (X, Y) with identical Stark shift behavior separated by the FSS energy (6.8 GHz for this QD). These two exciton transitions have orthogonal linear polarizations, however, their orientation is typically not aligned with the polarization of the cavity. Therefore, (i) we can study them both with the resonant Stark spectroscopy, and (ii) they couple to both cavity modes. Importantly, the same transition lines are identified also if the excitation and detection polarizations are swapped, see Fig. 2.4(a,b).

The optical selection rules of the negatively charged QD, on the other hand, allow in the absence of the external magnetic field only energy-degenerate emission of a circularly polarized photon with a helicity depending on the orientation of the spin in the ground state. Thus, we expect to detect a single emission line independently of the excitation polarization, in agreement with the observation in Stark spectroscopy presented in Fig. 2.4(c,d).

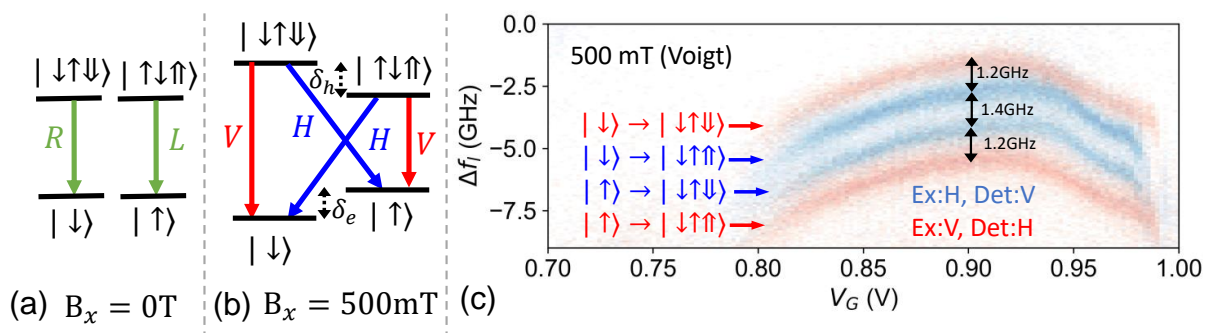### 2.3.2 Resonant spectroscopy in an in-plane magnetic field

Figure 2.5: Negative trion in an in-plane magnetic field. Energy levels with optical selection rules of negatively charged QD without (a) and with (b) in-plane magnetic field. c) Resonant spectroscopy of negatively charged QD in 500 mT in-plane magnetic field. We compare resonant fluorescence spectra measured in cross-polarization for two orthogonal excitation laser polarizations: H (blue) and V (red). The detected lines are labeled according to the optical selection rules.

Another technique we use to identify trion transitions is based on mapping its spin

configuration in a weak ($< 1\,\mathrm{T}$) external in-plane (Voigt geometry) magnetic field. In the magnetic field, initially energy degenerate X^- transitions [Fig. 2.5(a)] are split into two pairs of separated (by Zeeman splitting) lines with orthogonal linear polarization [98], shown in Fig. 2.5(b). Experimentally, we again use Stark spectroscopy with cross-polarization detection to block the reflected excitation laser and monitor the weak QD emission as a function of bias voltage V_G, shown in Fig. 2.3(c). In this figure, we see superimposed two data sets measured with the polarization of the excitation laser aligned to V- (H-) cavity mode. We observe two "red" lines surrounding two "blue" transitions, where the color encoding represents the excitation polarization. This ordering and mutual splitting of $1.4\,\mathrm{GHz}$ and $3.8\,\mathrm{GHz}$ between the lines is characteristic of a trion with electron and hole g-factors $|g_\mathrm{e}| = 0.18$ and $|g_\mathrm{h}| = 0.40$. In contrast, the emission of X^0 would show only two bright lines separated already without a magnetic field by fine-structure splitting (FSS) given by QD symmetry [98, 99].
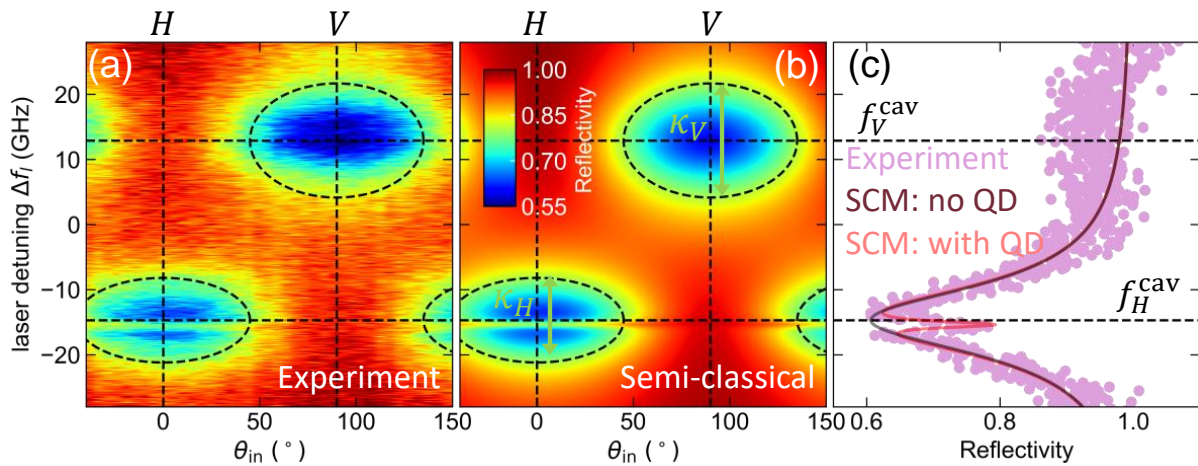
2.3.3 Semi-classical model

Figure 2.6: Analysis of cavity reflection as a function of laser detuning and linear input polarization. The two false-color plots show (a) experimental data and (b) polarized semi-classical theory results based on [90]. The cross-section plot in (c) compares measured data with excitation polarization direction along the H cavity mode (blue symbols) with a semi-classical model fit with (red) and without (black) QD in cavity resonance. Ellipses highlight the cavity mode resonances: resonant frequencies are shown as horizontal lines, cavity eigenpolarizations as vertical lines, and semi-minor axis is given by κ.

Another method we often use to identify the spin state of a QD coupled to a cavity is based on careful analysis of the cavity reflection as a function of excitation linear polarization direction. For the analysis, we use a semi-classical model derived in the weak coupling "bad-cavity" regime ($g \ll \kappa$) extended with the Jones formalism, allowing to include polarization effects such as cavity birefringence and optical selection rules of the QD transitions [90]. We focus on QD interaction with orthogonally polarized fundamental cavity modes with resonant frequencies $f_H^\mathrm{cav}, f_V^\mathrm{cav}$ and cavity loss rates κ_H, κ_V, where the total transmission matrix of the QD-cavity system is given by

$$t_\mathrm{tot} = \eta_\mathrm{out} \left[\begin{pmatrix} 1 - 2i\Delta_H & 0 \\ 0 & 1 - 2i\Delta_V \end{pmatrix} + R_{-\theta_\mathrm{QD}} X R_{\theta_\mathrm{QD}} \right]^{-1}. \tag{2.1}$$

Here, the interaction between the laser light and cavity modes is described by the first term using the normalized laser detuning $\Delta_m = (f_l - f_m^{\text{cav}})/\kappa_m$, for $m = H, V$, where f_l is the laser frequency of the scanning laser across the cavity modes. The interaction of the cavity and the QD is included in a transmission matrix X, which is diagonal in the QD polarization basis and carries information about the QD transition optical selection rules. In general, the QD-cavity interaction induces frequency-dependent phase shift $\phi = 2C/(1 - i\Delta^{\text{QD}})$ on the light transmitted by the cavity [100]. Here, we define the normalized laser detuning $\Delta^{\text{QD}} = (f_l - f^{\text{QD}})/\gamma_\perp$ with respect to the QD resonance frequency f^{QD}, dephasing rate $\gamma_\perp = \frac{\gamma_\parallel}{2} + \gamma^*$, and the cooperativity parameter $C = \frac{g^2}{\kappa\gamma_\perp}$ describing QD-cavity interaction with coupling strength g. Using Jones vectors to describe the QD polarization selection rules, the matrix for the doublet of the neutral exciton can be represented as $X_{X^0} = \begin{pmatrix} \phi_H & 0 \\ 0 & \phi_V \end{pmatrix}$ and $X_{X^-} = \begin{pmatrix} \phi_\sigma & 0 \\ 0 & \phi_\sigma \end{pmatrix}$ in case of negative trion. Finally, because of possible misalignment of the dipole axes of the QD transitions and the cavity polarization basis, X is rotated to the cavity polarization frame by the 2D rotation matrix $R_{\theta_{\text{QD}}}$, where θ_{QD} is the angle between the cavity and QD linear polarization frames. This frame rotation is essential for the correct description of X^0 doublet, as discussed in detail in Ref. [90]. η_{out} is the probability amplitude that a photon leaves the cavity through one of the mirrors.

Experimentally, we usually measure the cavity reflection as a function of excitation linear polarization orientation. Typical data are shown in Fig. 2.6. Here, we control the linear polarization of the excitation laser by rotation of a half-wave plate, relative to the initial laser polarization. For each half-wave plate angle $\theta_{\text{in}}/2$, we measure with a single-photon detector the reflection as a function of laser detuning, this time without the polarizer in the detection path. Theoretically, the initial polarization can be described by a Jones vector $\mathbf{e}_{\text{in}} = (\cos\theta_{\text{in}}, \sin\theta_{\text{in}})^T$ and measured as $R = 1 - |t_{\text{tot}}\mathbf{e}_{\text{in}}|^2$.

In Fig. 2.6(a), we recognize two elliptical reflection dips if the laser is on-resonance with the fundamental cavity modes. As expected, the cavity modes have linear and orthogonal polarization (H and V polarization) and show energy splitting by shape- and strain-induced birefringence by $f_H^{\text{cav}} - f_V^{\text{cav}} = 29.4 \pm 0.1\,\text{GHz}$. Further, the H-polarized cavity mode is intersected by a QD transition. Because we observe only a single line with emission independent of the linear excitation polarization, we identify this transition as negative trion X^-.

Now, we fit the experimental data to the polarized semi-classical model [90] and determine all relevant parameters of the cavity-QD device. First, from measurement with the QD detuned from the cavity resonance (not shown), we determine decay rates of both cavity modes: $\kappa_V = 17.5 \pm 0.3\,\text{GHz}$ and $\kappa_H = 13.0 \pm 0.3\,\text{GHz}$. Keeping the cavity decay rates fixed, we repeat the analysis with a trion transition on resonance with the H-polarized cavity mode and find a QD relaxation rate of $\gamma_\parallel = 1.4 \pm 0.3\,\text{GHz}$, negligible pure dephasing, and QD-cavity coupling constant $g = 1.4 \pm 0.1\,\text{GHz}$.

2.4 Single-photon emission

Finally, we show that our devices function as single-photon emitters. First, we set the excitation polarization and operating bias voltage such that we resonantly excite a trion transition, shown in Fig. 2.4(c). Second, we use a cross-polarization detection scheme to separate the QD resonant fluorescence (RF) from the continuous-wave excitation laser [101] and collect the RF photons in single-mode fiber. We measure the second-order
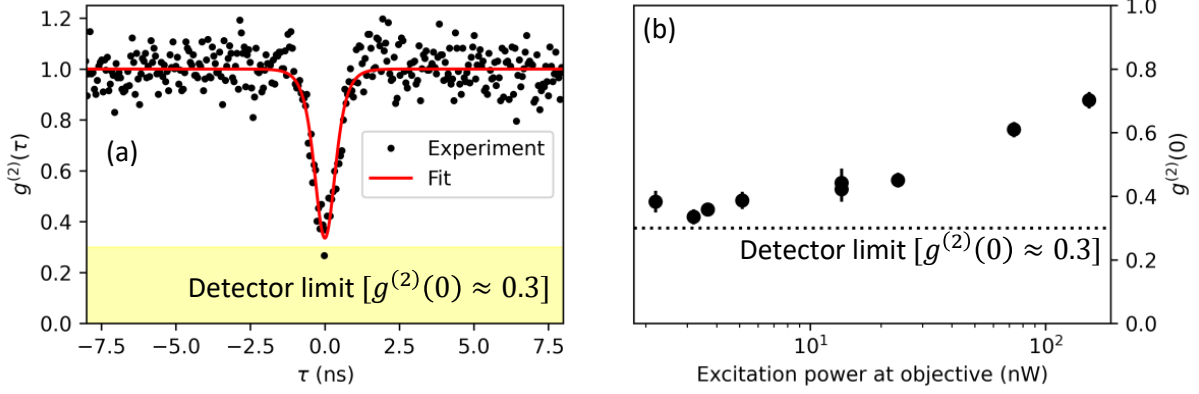
Figure 2.7: Second-order correlation function measured by continuous-wave excitation of a singly-charged QD. (a) Two-photon correlations $g^{(2)}(\tau)$ measured as a function of delay time τ between coincidence clicks. At low excitation power ($3\,\text{nW}$) and $\tau = 0$, we observe anti-bunching dip with $g^{(2)}(0) = 0.34 \pm 0.2$. (b) Dependency of $g^{(2)}(0)$ on excitation power.

correlation function $g^{(2)}(\tau)$ with Hanbury-Brown & Twiss (HBT) experiment, where RF is split by a fiber splitter connected to two single-photon detectors registering photon clicks with detection delay τ. Figure 2.7(a) shows the normalized $g^{(2)}(\tau)$ measured with a continuous stream of photons. The correlation function shows a dip at time delay $\tau = 0$ with the raw value of $g^{(2)}(0) = 0.34 \pm 0.02$, a clear signature of a single-photon source. However, because the two-detector jitter of $532\,\text{ps}$ is of the same order as the Purcell-enhanced QD emission, the measured dip does not reach $g^{(2)}(0) = 0$ of perfect single-photon source, but its minimum is limited to $g^{(2)}(0) \approx 0.3$. We compare the measured photon correlations with the theoretical curve expected for a perfect single-photon source convolved with the Gaussian instrument response function [18].

Figure 2.7(b) shows $g^{(2)}(0)$ extracted from the experiment as a function of excitation power. In principle, if the detection polarizer could block all residual laser light, a perfectly pure single-photon stream independent of the excitation power (if well below saturation) is expected. However, in our experiments, we achieve polarization extinction around 4×10^6 and a single-photon contrast, i.e., the signal of QD compared to the background, of only about 30. Therefore, with increasing excitation power, the fraction of unblocked laser light contaminating our single photon stream is increasing. This results in lower single-photon purity measured as $1 - g^{(2)}(0)$.